Collisional excitation of C2H and C2D by molecular hydrogen

Paul Pirlot, François Lique, P J Dagdigian

MNRAS 000, 1–9 (2015) Preprint 13 September 2023 Compiled using MNRAS LATEX style file v3.0

Collisional excitation of C_2H and C_2D by molecular hydrogen

P. Pirlot Jankowiak,[1] F. Lique,[1]★ and P. J. Dagdigian[2]
[1]*Univ Rennes, CNRS, IPR (Institut de Physique de Rennes) - UMR 6251, F-35000 Rennes, France*
[2]*Department of Chemistry, The Johns Hopkins University, Baltimore, MD 21218-2685, USA*

Accepted XXX. Received YYY; in original form ZZZ

ABSTRACT

The determination of physical conditions in interstellar clouds requires reliable estimation of radiative and collisional data for molecules detected in space. In this work, rate coefficients for (de-)excitation of C_2H and C_2D induced by collisions with both *ortho*- and *para*-H_2 are presented. Calculations have been carried out using a recently published four dimensional C_2H–H_2 potential energy surface. Fine structure resolved cross sections were computed with the time-independent close-coupling approach. We report cross sections for transitions between the first 41 levels of C_2H and corresponding rate coefficients up to 500 K. We also computed cross sections for transitions between the first 31 levels of C_2D and corresponding rate coefficients up to 200 K. Then, hyperfine structure resolved cross sections and rate coefficients were computed using the recoupling technique. The hyperfine structure resolved rate coefficients for C_2H–H_2 and C_2D–H_2 are calculated for the first 38 hyperfine C_2H energy levels and first 55 hyperfine C_2D energy levels both for temperatures up to 100 K. These collisional data were used in a simple radiative transfer modeling.

Key words: molecular data – radiative transfer – scattering

1 INTRODUCTION

The ethynyl radical C_2H was first detected by Tucker et al. (1974) in the interstellar medium (ISM) through the $n = 1 \rightarrow 0$ rotational line. Later, experimental studies (Sastry et al. 1981; Gottlieb et al. 1983) reported spectroscopic measurements for the $n = 2 \rightarrow 1$ and $n = 3 \rightarrow 2$ lines, providing accurate spectroscopic data for the $X^2\Sigma^+$ electronic state of this radical. Since then, C_2H has been detected in a wide range of astrophysical environments such as molecular clouds (Wootten et al. 1980; Sakai et al. 2010), star-forming regions (Beuther et al. 2008; Treviño-Morales et al. 2014; Yoshida et al. 2019), prestellar cores (Padovani et al. 2009), protoplatenary disks (Dutrey et al. 1996) and photodissociation regions (PDRs) (Ziurys et al. 1982; Teyssier et al. 2003; Cuadrado et al. 2015; Nagy et al. 2015) and is one of the most abundant hydrocarbon molecules in the ISM.

Also, the high abundance of C_2H in the ISM makes possible the observation of its deuterated isotopologue C_2D. Indeed, the first detection of the C_2D radical in the ISM was reported by Combes et al. (1985) in the Kleinman-Low nebula through the $n = 3 \rightarrow 2$ rotational line. This observation was corroborated by two parallel laboratory studies (Vrtilek et al. 1985; Bogey et al. 1985). This isotopologue has been subject to additional detections in molecular clouds (Turner 2001), PDR (Parise et al. 2009) and star-forming regions (Treviño-Morales et al. 2014).

The abundance ratio between hydrogenated and deuterated molecules is usually found to deviate from the cosmological elemental ratio [D/H] $\sim 2 \times 10^{-5}$ (Linsky et al. 2006). This abundance ratio can vary by several orders of magnitude from a source to another and also on the molecule, since the abundance of a molecule depends on its formation path and on the physical conditions of the medium. An accurate determination of the abundance of C_2H and C_2D is of interest to better understand and constrain the deuteration fraction in the ISM. That can give an insight on the evolution of molecular clouds, the abundance of deuterated molecules showing to strongly depend on the age of these objects in chemical models (Treviño-Morales et al. 2014).

The knowledge of the physical conditions of the ISM and especially molecular abundances relies on the interpretation of observational spectra through radiative transfer modeling. Notwithstanding, interstellar environments are subject to low density and energy levels of the detected molecules are out of the local thermodynamic equilibrium (LTE) (Roueff & Lique 2013). Then, it is necessary to study excitation mechanisms including both radiative and collisional processes. On one hand, radiative mechanisms are related to Einstein coefficients which depend on the dipole moment of the molecule involved and are determined through spectroscopic analysis. On the other hand, collisional processes are quantified by rate coefficients and can be determined through (quantum) calculations for a given collisional system. It is then of interest to study the excitation of both C_2H and C_2D with molecular hydrogen which is the main collider in molecular clouds where these two isotopologues are mainly observed.

The first collisional study implying C_2H target was done by Spielfiedel et al. (2012), providing fine and hyperfine rate coefficients for transitions induced by He as a substitute of H_2. Najar et al. (2014) provided rate coefficients up to 100 K for the C_2H-*para*-H_2 collisional system, taking into account only the fine structure splitting of

★ E-mail: francois.lique@univ-rennes.fr

C_2H. To do so, they computed a potential energy surface (PES) based on the rigid rotor approximation, considering *para*-H_2 as a pseudo-atom. This approach excluded the contribution of excited levels of H_2($j_2 \geq 1$, j_2 being the rotational state of H_2) in the scattering calculations. This potential has also been used by Dumouchel et al. (2017) to compute hyperfine resolved rate coefficients of C_2H and C_2D with *para*-H_2 up to 80 K. In a more recent work, Dagdigian (2018a) used the coupled cluster theory to compute a new 4D PES of the C_2H–H_2 collisional system. This author employed this PES to provide hyperfine rate coefficients of C_2H with *para*-H_2 and the first collisional data with *ortho*-H_2 up to 300 K (Dagdigian 2018b). A reasonable agreement was found with the work from Najar et al. (2014) for C_2H–*para*-H_2 fine structure resolved rate coefficients. The differences between these results mostly come from the size of H_2 rotational basis in scattering calculations. One can expect that these discrepancies would impact results for the C_2D–H_2 collisional system as well, and new calculations with the 4D PES can be useful.

As far as we know, there are no data about collisional excitation of C_2D with *ortho*-H_2. Such data are necessary for modeling environments where *ortho*-H_2 is significantly populated (Treviño-Morales et al. 2014). The purpose of this paper is to fill this lack of data. We report the first hyperfine resolved rate coefficients for C_2D collisions with *ortho*-H_2 and improved C_2D–*para*-H_2 collisional data up to 100 K using the 4D PES computed by Dagdigian (2018a). We also recompute hyperfine resolved rate coefficients for the C_2H–H_2 collisional system up to 100 K.[1] We also extend the range of temperature of fine structure C_2H–H_2 collisional data up to 500 K. New fine structure rate coefficients have been computed for the C_2D–H_2 collisional system up to 200 K. These data are expected to cover the temperature range of environments where C_2H and C_2D are detected (Nagy et al. 2015; Treviño-Morales et al. 2014).

The paper is organised as follows: Sec 2 presents the features of the potential energy surface used in scattering calculations and how to make it suitable for molecular dynamics of the C_2D–H_2 collisional system. State-to-state de-excitation rate coefficients of both C_2H and C_2D in collision with molecular hydrogen are presented in Sec 3 (It should be noted that excitation rate coefficients can be obtained from the de-excitation rate coefficients through detailed balance). As an application of this new data, we perform a simple radiative transfer application in Sec 4. A conclusion summarises this work in Sec 5.

2 METHODOLOGY

2.1 Potential energy surface

The potential energy surface (PES) describing the electronic interaction of the C_2H–H_2 collisional system has been computed by one of the authors of the present paper (Dagdigian 2018a). This author used the restricted coupled cluster formalism including single, double and (perturbative) triple excitations [RCCSDT] (Knowles et al. 1993) to perform *ab initio* calculations using the MOLPRO software (Werner et al. 2020). The aug-cc-pVQZ basis set (Dunning 1989) was used to ensure convergence of the interaction potential around the global minimum. The interaction energy of the bimolecular complex depends on four degrees of freedom: The separation R between the centers of mass of C_2H and H_2 PES; the angle θ_1 between the C_2H internuclear axis and the Jacobi vector **R**; the angle θ_2 between the H_2 internuclear axis and the Jacobi vector **R**; and the dihedral angle ϕ between the (C_2H,**R**) plane and H_2 axis. Both C_2H and H_2 are considered as rigid rotors, where their nuclear geometries are taken as their respective equilibrium configurations in the ground vibrational state.

[1] It has been found that the most recent available collisional data (Dagdigian 2018b) was overestimated by a factor ~ 1.4. Also, we figured out a bug in the recoupling approach from the scattering software used in this work did not correctly calculate quasi-elastic transitions.

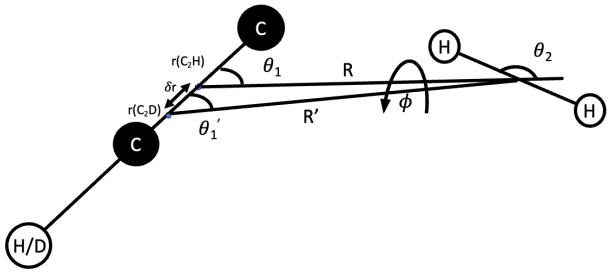

Figure 1. Representation of the C_2H–H_2 and C_2D–H_2 geometries. The unprimed and primed quantities refer to C_2H and C_2D respectively.

The fit of the PES was represented by an expansion in bispherical harmonics:

$$V(R,\theta_1,\theta_2,\phi) = \sum_{l_1 l_2 l} v_{l_1 l_2 l}(R) A_{l_1 l_2 l}(\theta_1,\theta_2,\phi) \quad (1)$$

The $A_{l_1 l_2 l}(\theta_1,\theta_2,\phi)$ in Eq. 1 depend on the angular coordinates of the system, defined as:

$$A_{l_1 l_2 l}(\theta_1,\theta_2,\phi) = \left(\frac{[l_1]}{4\pi}\right)^{1/2} \sum_m (l_1 m l_2, -m|l0) \times Y_{l_1 m}(\theta_1,0) Y_{l_2,-m}(\theta_2,\phi) \quad (2)$$

where the Y_{lm} are spherical harmonics, (....|..) are Clebsch-Gordan coefficients, $[x] \equiv (2x+1)$. The $v_{l_1 l_2 l}(R)$ are the radial coefficients for a given distance R, and l_1, l_2, l are chosen such that $|l_1 - l_2| < l < l_1 + l_2$. Eqs. 1 and 2 are the most suitable form of the PES for time-independant scattering calculations. The global minimum was found for $R = 7.82a_0$ and the $\theta_1 = 180°$, $\theta_2 = 90°$, $\phi = 0°$ orientation with an associated well depth D_e of 133.4 cm^{-1}.

Within the Born-Openheimer approximation, it is possible to use the C_2H–H_2 PES to describe the interaction of the C_2D–H_2 complex. This can be performed with a transformation of the coordinates through a shift δr of the center of mass of the targeted molecule (see Fig. 1). The transformation from one isotopologue frame to the other one can be obtained through:

$$\delta r = r(C_2D) - r(C_2H) \quad (3)$$

$$R' = \sqrt{R^2 + \delta r^2 + 2R\delta r \cos(\theta_1)} \quad (4)$$

$$\theta_1' = \cos^{-1}\left(\frac{R\cos(\theta_1) - \delta r}{R'}\right) \quad (5)$$

where $r(C_2H)$ and $r(C_2D)$ are the positions of the center of mass of C_2H and C_2D respectively along the internuclear axis (see Fig. 1). The same bond lengths are assumed for C_2D than for C_2H since the molecule is assumed to be rigid. The transformation of the coordinates θ_2 and ϕ was not necessary since the impact on the dynamics is found to be negligible. The center of mass is shifted by $\delta r = +0.1157a_0$, toward the deuterium end. This transformation leads to a new expansion of the PES for the C_2D–H_2 complex. Dagdigian (2018a) obtained a fit for $l_1 = 12$ and $l_2 = 6$, leading to 174 radial coefficients for C_2H–H_2. For the C_2D–H_2 collisional system, we expanded the PES with the same number of coefficients as for C_2H–H_2 using a Gauss-Legendre quadrature with 686 geometries.

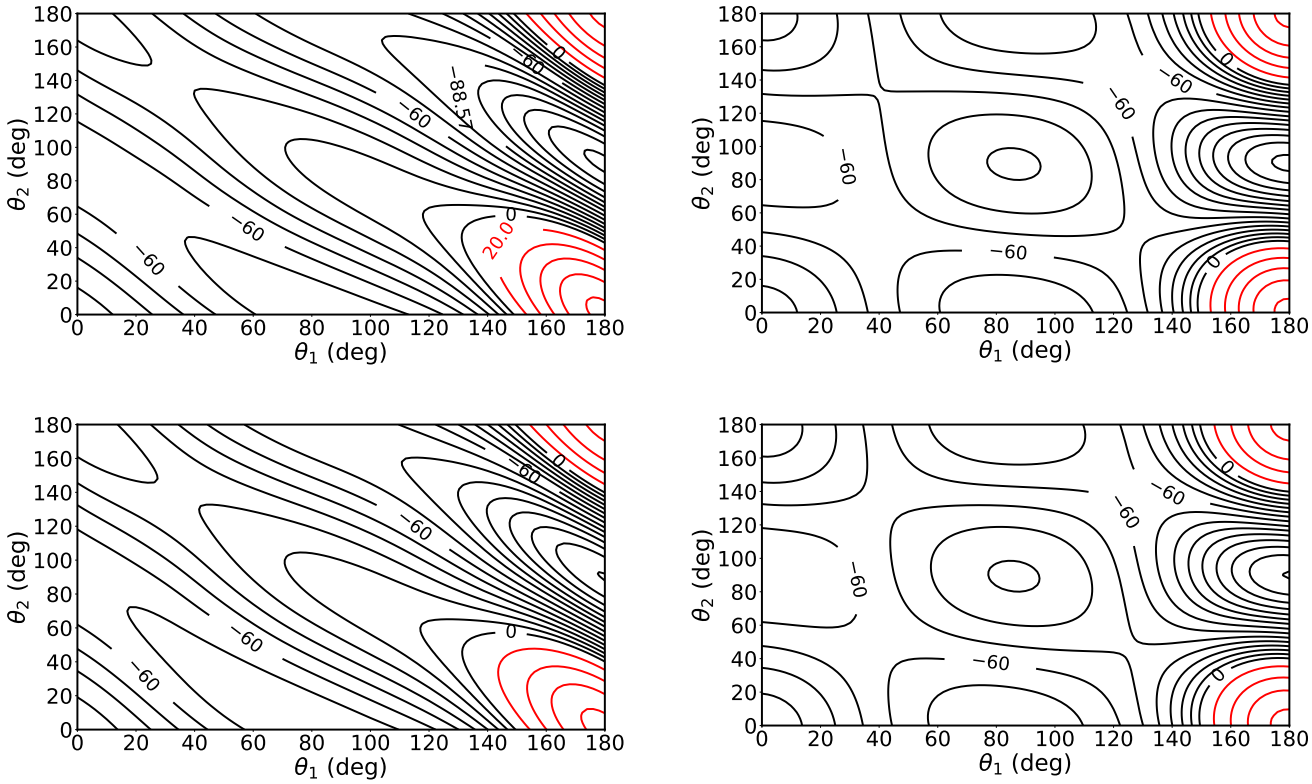

Figure 2. Contour plots of the interaction potential of C_2H (upper panels) and C_2D (lower panels) for an intermolecular separation $R = 7.82a_0$. The left and right panels have $\phi = 0°$ (left panels) and 30° (right panels). Contours in red represent a repulsive interaction, contours in black an attractive interaction. The values of the potential are given in cm^{-1}.

It is interesting to check the impact of the isotopic substitution on the contour plots of the PES for given geometries. Figure 2 shows the angular dependence of the PES of the C_2H–H_2 and C_2D–H_2 complexes for two geometries around the global minimum. One can see that for both isotopologues, the most repulsive interaction occurs when $\theta_1 = 180°$, corresponding to the orientation of the targeted hydrogen/deuterium toward the collider, and for $\theta_2 = 0°$ and $\theta_2 = 180°$.

The most attractive part of the PES corresponds to a T-shaped structure of the complexes ($\theta_1 = 180°$, $\theta_2 = 90°$), where the global minimum is reached. These contour plots illustrate the large anisotropy of the PES. Even if the shapes of the interaction energy look very similar in both isotopologue frames, one can see slight differences in the range $\theta_1 = 140 - 180°$, where larger anisotropy is seen for the C_2H–H_2 complex. Such differences will have impact on the magnitude of the C_2H–H_2 and C_2D–H_2 excitation cross sections as will be seen in Sec 3.

2.2 Scattering formalism

Both C_2H and C_2D are open-shell molecules with a $^2\Sigma^+$ electronic ground state. The unpaired electron, with spin $S_1 = 1/2$, couples with the rotational angular momentum n_1 to yield the total angular momentum j_1 of the molecule:

$$\mathbf{n}_1 + \mathbf{S}_1 = \mathbf{j}_1$$

During the collision, j_1 and the rotational angular momentum j_2 of the projectile will be coupled with the rotation of the target. The total angular momentum J of the complex thus equals

$$\mathbf{J} = \mathbf{j}_{12} + \mathbf{L}$$

where $\mathbf{L}$ is the orbital angular momentum and $\mathbf{j}_{12} = \mathbf{j}_1 + \mathbf{j}_2$ is the vector sum of the molecular angular momenta. This coupling scheme has been used in quantum time-independent calculations with the close coupling method (CC) to determine fine-structure resolved cross sections in the same way as employed by Dagdigian (2018b).

In addition, both C_2H and C_2D possess a nonzero nuclear spin due to the H and D nuclei. The coupling of the nuclear spin to the rotation yields a hyperfine splitting of the fine-structure energy levels where

$$\mathbf{F}_1 = \mathbf{j}_1 + \mathbf{I}_X$$

where F_1 denotes the total angular momentum of the targeted isotopologue including its nuclear spin, I_X is the nuclear spin (X = H or D), $I_H = 1/2$, and $I_D = 1$. When the hyperfine splittings are small, it is possible to consider them as degenerate and carry out hyperfine structure calculations using a recoupling technique (Alexander & Dagdigian 1985). Then, the nuclear spin can be recoupled to the total angular momentum of the complex as $J + I_X = J_T$.

This approach consists of using nuclear spin-free T-matrix elements $T^J_{n_1 j_1 j_2 j_{12} L, n_1' j_1' j_2' j_{12}' L'}$ computed by the CC method to determine hyperfine resolved cross sections. The T-matrix elements in-

cluding the nuclear spin can be obtained using the spin-free T-matrix elements (Offer et al. 1993):

$$
\begin{aligned}
T^{J_T}_{n_1 j_1 F_1 j_2 j_R L, n'_1 j'_1 F'_1 j'_2 j'_R L'} &= \sum_{J j_{12} j'_{12}} (-1)^{j_2+j'_2+j_R+j'_R+L+L'} \\
&\times \left([j_{12}][j'_{12}][j_R][j'_R][F_1][F'_1]\right)^{1/2} [J] \\
&\times \begin{Bmatrix} j_1 & j_2 & j_{12} \\ L & J & j_R \end{Bmatrix} \begin{Bmatrix} j'_1 & j'_2 & j'_{12} \\ L' & J & j'_R \end{Bmatrix} \\
&\times \begin{Bmatrix} j_R & j_1 & J \\ I_X & J_T & F_1 \end{Bmatrix} \begin{Bmatrix} j'_R & j'_1 & J \\ I_X & J_T & F'_1 \end{Bmatrix} \\
&\times T^{J}_{n_1 j_1 j_2 j_{12} L, n'_1 j'_1 j'_2 j'_{12} L'} \qquad (6)
\end{aligned}
$$

Here, $j_2 + L = j_R$ and $j_R + F_1 = J_T$. The T-matrix elements in Eq. 6 can be used to compute hyperfine resolved cross sections:

$$
\begin{aligned}
\sigma_{n_1 j_1 F_1, n'_1 j'_1 F'_1} &= \frac{\pi}{k^2 [F_1][j_2]} \\
&\times \sum_{J_T j_R j'_R L L'} [J_T] \left| T^{J_T}_{n_1 j_1 F_1 j_2 j_R L, n'_1 j'_1 F'_1 j'_2 j'_R L'} \right|^2 \qquad (7)
\end{aligned}
$$

where k^2 is the wave vector of the initial state.

Nuclear spin-free calculations have been carried out for C_2D collisions with both *ortho*- and *para*-H_2 up to 1618.7 cm^{-1} and 1500 cm^{-1}, respectively, for energy levels up to $n_1 \leq 15$ (see Appendix A for more details about the used parameters in scattering calculations). These calculations have been performed including a rotational basis of $j_2 = 0, 2$ for *para*-H_2. In the case of *ortho*-H_2 collisions, only a basis $j_2 = 1$ was necessary.

For collisions of C_2D with *ortho*-H_2 and *para*-H_2, hyperfine rate coefficients have been computed for 55 energy levels up to $n_1 = 9$ and for temperatures between 5 and 100 K. For the C_2H–H_2 collisional system, fine-structure calculations were performed up to a total energy of 3500 cm^{-1} for collisions with *para*-H_2 and 3618.7 cm^{-1} for collisions with *ortho*-H_2. Energy levels with n_1 up to 20 were taken into account in the CC calculations. Fine-structure rate coefficients were then computed up to 500 K. All scattering calculations (both CC and recoupling) were performed with the HIBRIDON scattering code (Alexander et al. 2023). For the highest total energies considered, greater than 1500 cm^{-1}, the convergence of cross sections with respect to the H_2 basis used is moderate, up to a few tens of percents of mean absolute deviation. Such intensive calculations may be accomplished by using the coupled state approximation. However, this method is not implemented yet in the HIBRIDON code for molecule-molecule collisions. However, this truncated H_2 basis moderatly impacts the rate coefficients presently computed.

The rate coefficient from an initial level i to a final level f consists in integrating the cross section in Eq. 7 over a Maxwell-Boltzmann distribution of the collisional energies E_c:

$$
k_{i\to f}(T) = \left(\frac{8}{\pi\mu(k_B T)^3}\right)^{1/2} \int_0^\infty \sigma_{i\to f}(E_c) E_c e^{-E_c/k_B T} dE_c \qquad (8)
$$

where μ is the reduced mass of the given collisional system and k_B is the Boltzmann's constant.

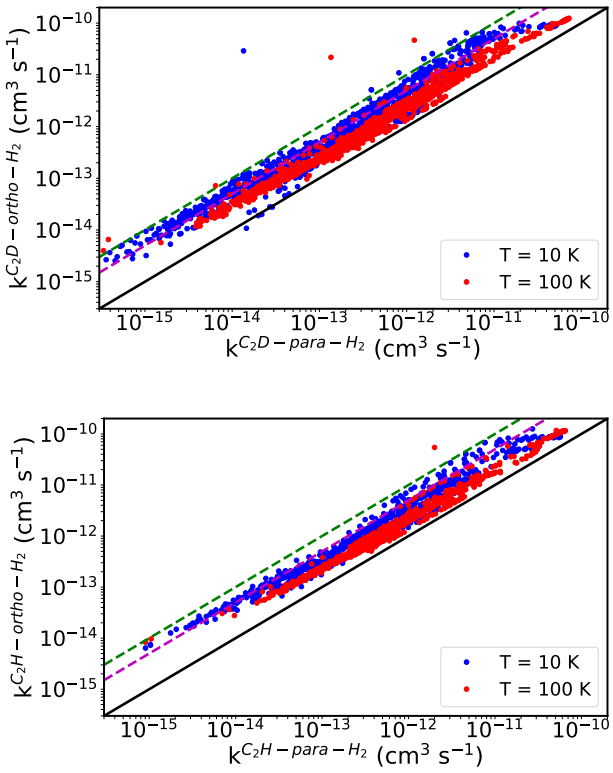

Figure 3. Systematic comparison of hyperfine rate coefficients for C_2D–*ortho*- and *para*-H_2 collisions (upper panel) and for C_2H–*ortho*- and *para*-H_2 collisions (lower panel) at 10 K and 100 K. Magenta and green dashed lines represent deviations within a factor of 5 and 10 respectively.

3 RATE COEFFICIENTS

3.1 C_2H–H_2 rate coefficients

Both fine and hyperfine structure resolved rate coefficients calculated in this work for the C_2H–H_2 collisional system are essentially the same with the same propensity rules as in the calculations by Dagdigian (2018b) and will not be discussed in details here. We just review the main features of these collisional data. It is found that the rate coefficients for collisions involving *ortho*-H_2 are larger than those with *para*-H_2 (see also Fig. 3). For fine structure transitions induced by *para*- and *ortho*-H_2, propensity rules (Alexander 1982) are observed for $\Delta n_1 = \Delta j_1$ transitions (see Fig. 6) with $\Delta n_1 = \Delta j_1 = 2$ transitions dominating over $\Delta n_1 = \Delta j_1 = 1$ transitions. These effects have an impact on the behaviour of hyperfine structure transitions, where fine structure conserving transitions displayed larger intensities for $\Delta j_1 = \Delta F_1$ transitions than for $\Delta n_1 \neq \Delta j_1$ ones.

3.2 C_2D–H_2 rate coefficients

Figure 3 shows a comparison between hyperfine resolved C_2D–*ortho*-H_2 and C_2D–*para*-H_2 rate coefficients at 10 K and 100 K. One can see that all rate coefficients are larger for C_2D–*ortho*-H_2 collisions by a factor of 10 at low temperatures. Such deviations come from the PES features, where larger anisotropies are expected for the *ortho*-H_2 collider. These differences are still an order of a factor of 5 at 100 K. This also can be seen in Fig. 4, where *ortho*-H_2 rate coefficients are dominating the corresponding *para*-H_2 quantities. Such effect is well

known for neutral collisional systems such as PN–H_2 (Desrousseaux et al. 2021) or HC_2NC–H_2 and HNC_3–H_2 (Bop et al. 2021).

It is also possible to see a propensity rule in favor of fine-structure conserving ($\Delta n_1 = \Delta j_1$) transitions, which is consistent with results observed in C_2H collisions (Dagdigian 2018b). This propensity rules results from the fact that the electron spin is a spectator in the collision. This effect is generally observed for open-shell molecules such as CCS (Godard Palluet & Lique 2023), CN (Kalugina et al. 2013) or SH^+ (Dagdigian 2019). A propensity rule for even $\Delta n_1 = \Delta j_1$ transitions is observed.

More specifically, in the case of the hyperfine structure excitation, a propensity rule (Alexander & Dagdigian 1985) is also observed for $\Delta j_1 = \Delta F_1$ transitions. Similar to the propensity rule for fine-structure transitions, this hyperfine propensity rule results from the spectator role that nuclear spin plays in the collision. With the propensity rule for fine-structure transitions, the largest rate coefficients occur for $\Delta n_1 = \Delta j_1 = \Delta F_1$ transitions. The weakest transitions occur when $\Delta n_1 \neq \Delta j_1 \neq \Delta F_1$, sometimes by one order of magnitude compared to the dominant transitions.

It is interesting to compare the C_2D–H_2 rate coefficients with the previous study of Dumouchel et al. (2017). In their work, the 2D averaged PES computed by Najar et al. (2014) for the C_2H–H_2 collisional system and transformed to describe the C_2D–H_2 system was used for scattering calculations. The computed rate coefficients were computed with only $j_2 = 0$ in the H_2 rotational basis. Figure 5 shows a comparison between the two sets of collisional data for two given temperatures. One can see that most of the transitions are contained within a factor of 2 of differences, whereas the largest ones are relatively well reproduced. Such differences can come from several possibilities. First, the inclusion of two more degrees of freedom in the C_2H–H_2 interaction potential leads to more anisotropies (see Fig. 2) and radial coefficients to take into account in scattering calculations. Second, the inclusion of $j_2 = 0, 2$ rotational basis is often necessary to converge cross sections computed with the CC approach.

3.3 C_2H–H_2 vs C_2D–H_2 rate coefficients

Figure 6 presents comparisons of several fine-tstructure rate coefficients of C_2H and C_2D in collisions with both *ortho*- and *para*-H_2. It should be noted that the isotopologues have different numbers of hyperfine transitions because of the differences values of the H and D nuclear spins. The strongest impact of the isotopic substitution can be observed for $\Delta n_1 = \Delta j_1 = 1$ transitions for both H_2 colliders, in a more moderate way for *ortho*-H_2 than *para*-H_2. Such differences mostly come from the shift of the center of mass of the PES, leading to significant differences in expansion coefficients $v_{l_1 l_2 l}$. Especially, radial coefficients with odd l_1 indexes are larger for the C_2H–H_2 complex than the C_2D–H_2 one. This is related to the fact that the center of mass is closer of the center of the molecule in the case of C_2D and leads to less anisotropy in the PES (see Fig. 1).

For the other cases ($\Delta n_1 = \Delta j_1 = 2$ and $\Delta n_1 \neq \Delta j_1$), the impact of isotopic substitution is moderate and rate coefficients are of the same order of magnitude for both collisional systems. Since the PES expansion coefficients involved in the CC equations for these types of transitions are very similar, these slight differences can mostly come from the spectroscopic structure of the two targets since their rotational constant are quite different, where $B_{C_2H} = 1.457$ cm^{-1} and $B_{C_2D} = 1.203$ cm^{-1} (Gottlieb et al. 1983; Vrtilek et al. 1985).

4 EXCITATION OF C_2D IN THE ISM

Once hyperfine resolved rate coefficients are computed, it is possible to illustrate the impact of the new set of collisional data on radiative transfer modeling. Such modeling has already be done for the C_2H–H_2 collisional system (Dagdigian 2018b) and will not be discussed here. The following discussion will focus on the new data of the C_2D–H_2 collisional system. This was carried out using the RADEX code (Van der Tak et al. 2007) with the escape probability approximation. Calculations were performed in order to model typical cold environments where C_2D is detected, such as TMC-1 (Turner 2001) or L1527 (Yoshida et al. 2019). The kinetic temperature T_{kin} was set to 10 K, a linewidth of 0.5 km s^{-1}, and a typical column density of 1×10^{13} cm^{-2}. A background temperature T_{bg} was assumed to be 2.73 K, representing the Cosmic Microwave Background. Einstein coefficients were taken from the Cologne Database for Molecular Spectroscopy (CDMS) (Endres et al. 2016). Another calculation has been done at $T_{kin} = 50$ K to model warmer environments such as Monoceros R2 (Treviño-Morales et al. 2014), with a typical linewidth of 1 km s^{-1}.

Figure 7 shows the dependence of excitation temperatures upon the density of H_2 for several hyperfine transitions of the C_2D $n_1 = 1$–0 rotational line for kinetic temperature (T_{kin}) of 10 K and $n_1 = 2$–1 for $T_{kin} = 50$ K. The range of excitation temperature varies from $T_{ex} = T_{bg}$ at very low densities where radiative processes are dominant, to $T_{ex} = T_{kin}$ at high densities, where the LTE is reached due to the domination of collisional processes.

Comparisons were carried out with the set of data for C_2D–*para*-H_2 from Dumouchel et al. (2017). Also, the impact of the new *ortho*-H_2 collisions will be assessed with different *ortho*-to-*para*-H_2 ratio (OPR) taken for the radiative transfer calculations. For $T_{kin} = 10$ K, one can see that for 100% of *para*-H_2, excitation temperatures coincide with the kinetic temperature at $n_{H_2} \sim 2 \times 10^7$ cm^{-3}, showing that a very dense gas is needed to thermalize, whereas modeling obtained using Dumouchel et al. (2017) reaches LTE conditions at $n_{H_2} \sim 8 \times 10^6$ cm^{-3}. This is not surprising since most of rate coefficients for C_2D–*para*-H_2 of Dumouchel et al. (2017) are larger by up to a factor of 2, making collisions more efficient than the set of data provided in this work. However, most of the differences in this modeling are not more than 20%. The increasing of the OPR to 25% and 75% involves the contribution of C_2D–*ortho*-H_2 rate coefficients. It has an impact on the critical density because of the differences between *ortho*- and *para*-H_2 collisions. In addition, excitation temperatures of the presented transitions at $T_{kin} = 50$ K are less sensitive to *ortho*-H_2 collisions. For most of the models, LTE is reached around 10^6 cm^{-3}. That can also be related to the order of magnitude of the rate coefficients, having a strongly different behaviour at 10 K between *ortho*- and *para*-H_2 collisions than at higher temperatures (see Fig. 3) and be less sensitive to the modeling.

It is interesting to reinterpret C_2D observations made on L1527 by Yoshida et al. (2019) and to derive the C_2D column density with our new set of rate coefficients. We determined the column density range of C_2D by computing integrated intensity of different detected lines that best reproduce these observations (see Table 1), minimizing the following χ^2 parameter

$$\chi^2 = \sum_{i=1}^{N} \left(\frac{F_i^{obs} - F_i^{calc}}{\sigma_i} \right)^2 \quad (9)$$

where N denotes the number of observed lines, F_i^{obs} and F_i^{calc} are the integrated intensities observed and calculated respectively, and σ_i is the uncertainty of the i^{th} observation. We varied the

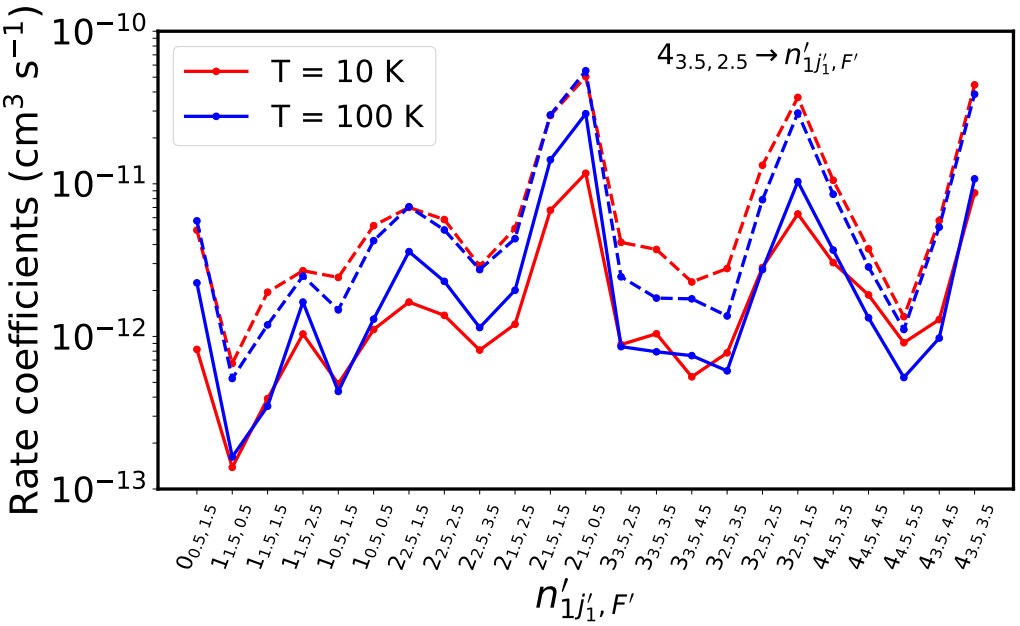

Figure 4. Hyperfine structure resolved transitions for C_2D in collision with *para*-H_2 (solid lines) and *ortho*-H_2 (dashed lines) from the $4_{3.5,2.5}$ energy level toward lower levels.

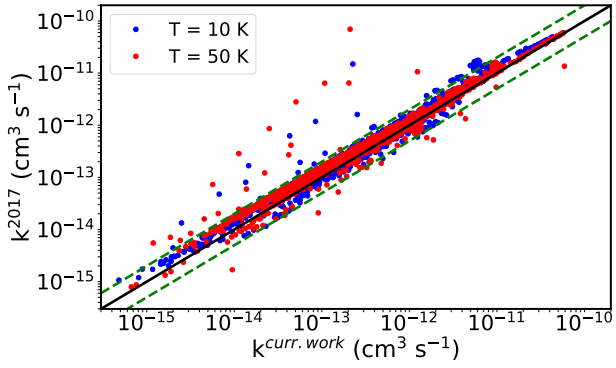

Figure 5. Systematic comparison of C_2D–*para*-H_2 hyperfine rate coefficients computed in this work and the previous study by Dumouchel et al. (2017) for transitions at 10 K and 50 K. Green dashed lines represent deviations within a factor of 2.

column density in the range $[10^{12} - 10^{14}]$ cm^{-2} and the H_2 density $[5 \times 10^5 - 3 \times 10^6]$ cm^{-3} for two fixed kinetic temperatures of 10 K and 15 K.

Figure 8 shows the dependence of the χ^2 parameter upon the H_2 density and the range of derived C_2D column densities for the best reproduced observations. One can see that for both kinetic temperatures, this procedure was not able to constrain the H_2 density within the proposed grid. For T_{kin} = 10 K, the column density is determined as $N = (3.2 - 4.9) \times 10^{13}$ cm^{-2} within a confidence level of 99%, where observations derived a value of $N = (4.7 \pm 0.3) \times 10^{13}$ cm^{-2}. For T_{kin} = 15 K, the column density is found to be $N = (3.6 - 5.8) \times 10^{13}$ cm^{-2} compared with observations where $N = (5.6 \pm 1.1) \times 10^{13}$ cm^{-2}. These calculations agree with the literature within a factor ~1.5 which is relatively consistant regarding the used methods and uncertainties involved. The column densities derived from observations were carried out in the LTE conditions, finding that lines are optically thin so no corrections need to be applied on brightness temperatures and used a least squares fitting method. In our calculations, the computed opacities are never greater than 0.1 for all lines and the two kinetic temperatures. However, it should be noted that the density influences excitation temperatures. The considered lines reproduced observations for excitation temperatures varying from ~11 to 13 K and from ~16 to 26 K for T_{kin} = 10 K and T_{kin} = 15 K respectively. This corresponds to a regime where lines are in a slight suprathermal effect and close to LTE conditions. Since the excitation temperatures do not match with the kinetic temperature, one can see that the derived ranges of column densities tends to decrease the observed values. Our best solutions where the χ^2_{min} is reached correspond to $N = 4.1 \times 10^{13}$ cm^{-2}, $n_{H_2} = 6 \times 10^5$ cm^{-3} and T_{ex} ~ 24 K for all hyperfine lines for T_{kin} =15 K. For the case where T_{kin} =10 K, χ^2_{min} is reached when $N = 3.7 \times 10^{13}$ cm^{-2}, $n_{H_2} = 6.5 \times 10^5$ cm^{-3} and T_{ex} ~ 13 K for the multiplet. This

Table 1. Line parameters for C_2D observations done by Yoshida et al. (2019)

Frequency (GHz)	Transition $(n_1, j_1, F) \rightarrow (n'_1, j'_1, F')$	$\int T_{mb} dv$ (K km s^{-1})
72.101715	(1,1.5,1.5) → (0,0.5,1.5)	0.147(16)‡
72.107700	(1,1.5,2.5) → (0,0.5,1.5)	0.395(16)
72.109114	(1,1.5,0.5) → (0,0.5,0.5)	0.117(14)
72.112399	(1,1.5,1.5) → (0,0.5,0.5)	0.144(15)
72.187704	(1,0.5,1.5) → (0,0.5,1.5)	0.165(20)
72.189505	(1,0.5,0.5) → (0,0.5,1.5)	0.12(3)
72.198388	(1,0.5,1.5) → (0,0.5,0.5)	0.065(16)

‡ Parenthesis represent the errors of last significant digits.

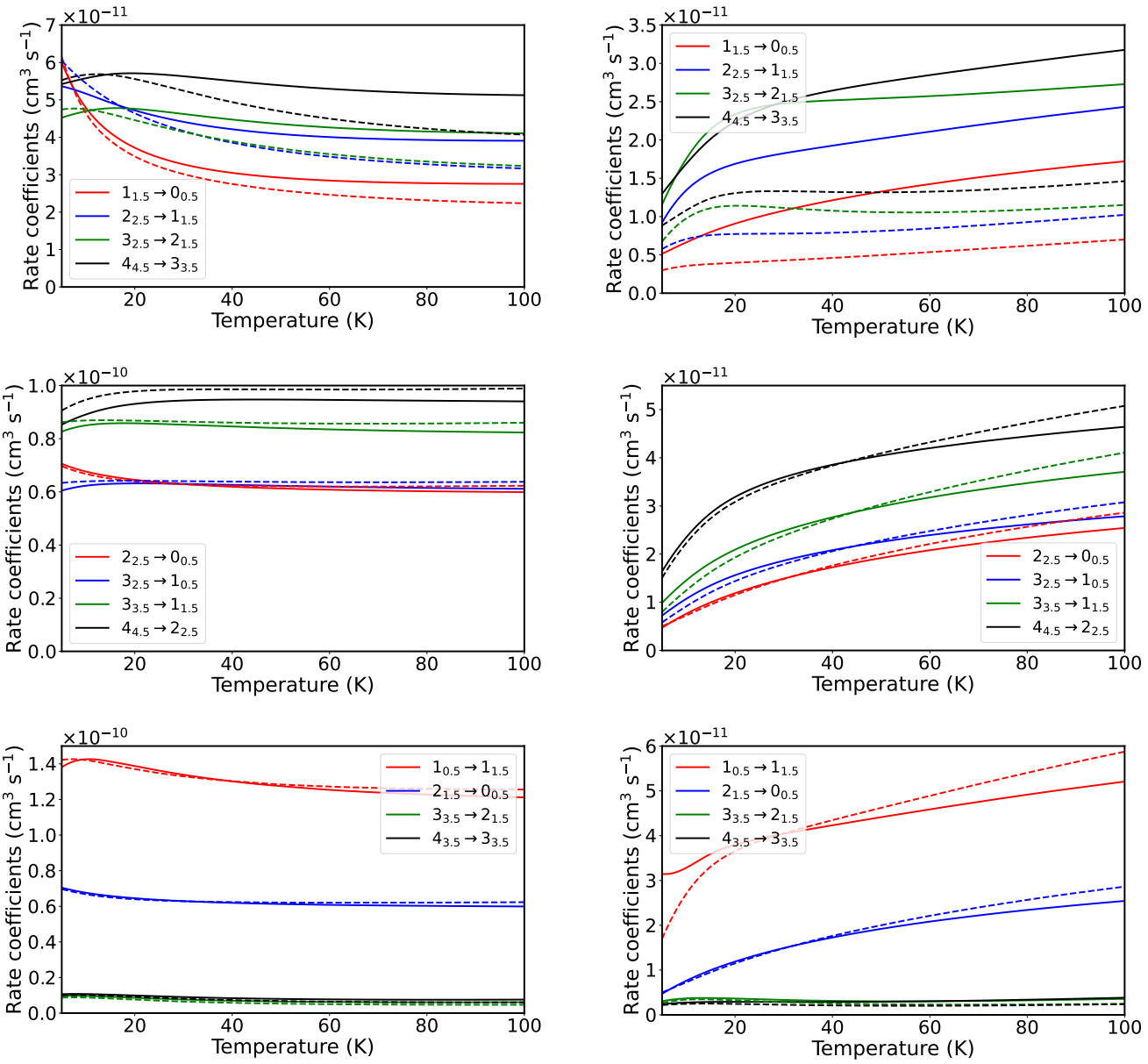

Figure 6. Temperature dependence of fine structure resolved rate coefficients for C_2H (solid lines) and C_2D (dashed lines) in collision with *ortho*-H_2 (left panel) and *para*-H_2 (right panel). Comparisons are done for $\Delta n_1 = \Delta j_1 = 1$ (upper), $\Delta n_1 = \Delta j_1 = 2$ (middle) and $\Delta n_1 \neq \Delta j_1$ (lower) transitions.

would mean that the population of these states under LTE conditions are underestimated compared to non-LTE modeling. In our case, we increase the population of the lower levels of these lines by $\sim$ 14% and $\sim$ 20% at $T_{\rm kin}$ =10 K and $T_{\rm kin}$ =15 K, respectively.

5 CONCLUSION

We computed hyperfine resolved rate coefficients for C_2H and C_2D in collision with both *ortho*- and *para*-H_2. These data take into account the first 38 C_2H hyperfine levels and the first 55 C_2D hyperfine levels up to 100 K. We also extended the range of temperature for fine structure C_2H–H_2 collisions up to 500 K for levels up to $n_1 = 20$. We also computed C_2D–H_2 fine structure resolved rate coefficients for levels up to n_1 = 15 and for temperatures up to 200 K. These data were computed using the 4D PES of Dagdigian (2018a) and the recoupling method (Alexander & Dagdigian 1985; Offer et al. 1993). C_2D–*ortho*-H_2 and C_2D–*para*-H_2 rate coefficients show very different behaviours, where differences are observed up to a factor of 10. This is a standard observation for neutral systems, showing the importance of taking into account the internal structure of H_2 in scattering calculations. We observed more specifically that fine-structure conserving transitions are larger than fine-structure changing ones for C_2D collisions and display even larger rate coefficients for the $\Delta n_1 = \Delta j_1 = \Delta F = 2$ propensity rule.

With isotopic substitution C_2H and C_2D rate coefficients can differ up to factor of 2 for $\Delta n_1 = \Delta j_1 = 1$ transitions, especially when collisions occur with *para*-H_2. For $\Delta n_1 = \Delta j_1 = 2$ transitions, both isotopologues with *ortho*- and *para*-H_2 are the same order of magnitude. Such results reflect the shift of the center of mass between the

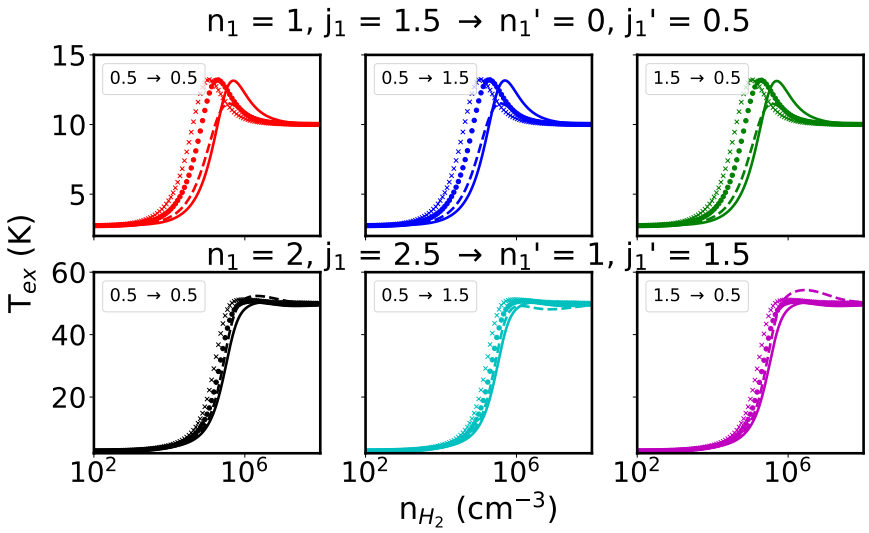

Figure 7. Excitation temperatures as a function of the density of H_2 at T_{kin} = 10 K (upper panels) and 50 K (lower panels) for several hyperfine radiative transitions of C_2D. Numbers in legend represent $F \rightarrow F'$ quantum numbers. Dashed lines are related to the set of data from Dumouchel et al. (2017), solid lines the set of data of the present work with 100% of *para*-H_2 density, dotted lines with 25% of *ortho*-H_2 and crossed lines with 75% of *ortho*-H_2.

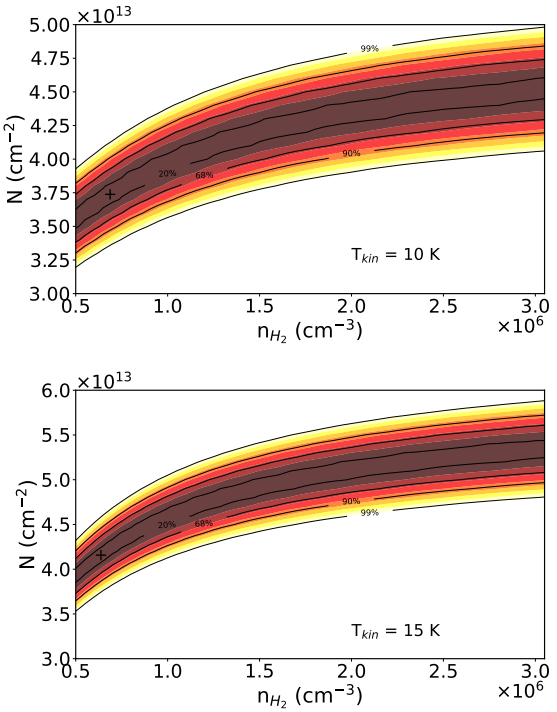

Figure 8. Dependance of the χ^2 parameter with the column density and the H_2 density for kinetic temperatures at 10 K (upper panel) and 15 K (lower panel). Values are shown for 20%, 68%, 90% and 99% levels of confidence representing χ^2_{min} + (0.45, 2.3, 4.61, 9.21) (Lampton et al. 1976; Schöier et al. 2002). The crossed dot represents the minimum of the χ^2.

two isotopologues in the PES, their energetic structure and the larger anisotropies of the PES for the *ortho*-H_2 collider.

This new set of data has been compared with the previous work done by Dumouchel et al. (2017), where they used a transformed 2D PES for the C_2D–H_2 system (*i.e* neglecting the internal structure of H_2). It has been shown that the inclusion of $j_2 = 0, 2$ in the rotational basis for scattering calculations lead differences up to a factor of 2.

We carried out a radiative transfer modeling to illustrate the impact of the new set of C_2D–H_2 rate coefficients. Differences in excitation temperatures are moderate between the new set of data and the one obtained by Dumouchel et al. (2017) compared to the usual uncertainties involved in astrophysical applications when only *para*-H_2 collisions occur. However, larger differences are observed when collisions with *ortho*-H_2 take place. We computed and reinterpreted the column density of C_2D under non-LTE conditions with the literature in the case of the low-mass star-forming region L1527 (Yoshida et al. 2019). The agreement with observations was found to be within a factor ∼1.5, which can be considered good regarding the uncertainties due to, on one hand, the methods used for calculations of the PES and rate coefficients, assumptions made by non-LTE modeling, and on the other hand uncertainties of the measurements and the methods used to compute column densities under the LTE assumption. Especially, LTE modeling are underestimating the population of the lower levels of a given transition compared to calculations done under non-LTE conditions.

These data are expected to be used for the interpretation of astronomical observations in order to determine physical conditions in regions where *ortho*-H_2 is significantly populated.

ACKNOWLEDGEMENTS

We acknowledge financial support from the European Research Council (Consolidator Grant COLLEXISM, Grant Agreement No. 811363). We wish to acknowledge the support from the CEA/GENCI (Grand Equipement National de Calcul Intensif) for awarding us access to the TGCC (Très Grand Centre de Calcul) Joliot Curie/IRENE supercomputer within the A0110413001 project.

DATA AVAILABILITY

Fine and hyperfine structure resolved rate coefficients for C_2H–H_2 and C_2D–H_2 will be available on the following databases: EMAA (https://dx.doi.org/10.17178/EMAA), LAMDA (Van der Tak et al. 2020) and BASECOL (Dubernet et al. 2012).

REFERENCES

Alexander M. H., 1982, J. Chem. Phys., 76
Alexander M. H., Dagdigian P. J., 1985, J. Chem. Phys., 83, 2191
Alexander M. H., Dagdigian P. J., Werner H. J., Kłos J., Desrousseaux B., Raffy G., Lique F., 2023, Computer Physics Communications, 289, 108761
Beuther H., Semenov D., Henning Th., Linz H., 2008, ApJ, 675, 33
Bogey M., Demuynck C., Destombes J. L., 1985, A&A, 144, 15
Bop C. T., Lique F., Faure A., Quintas-Sánchez E. L., Dawes R., 2021, Mon. Not. R. Astronom. Soc., 501, 1911
Combes F., Encrenaz P. J., Gerin M., Bogey M., Demuynck C., Destombes J. L., 1985, A&A, 147, 25
Cuadrado S., Goicoechea J. R., Pilleri P., Cernicharo J., Fuente A., Joblin C., 2015, A&A, 575
Dagdigian P. J., 2018a, J. Chem. Phys., 148
Dagdigian P. J., 2018b, Mon. Not. R. Astronom. Soc., 479, 3227
Dagdigian P. J., 2019, Mon. Not. R. Astronom. Soc., 487, 3427
Desrousseaux B., Quintas-Sánchez E. L., Dawes R., Marinakis S., Lique F., 2021, J. Chem. Phys., 154
Dubernet et al. M. L., 2012, A&A, 553, 50
Dumouchel F., Lique F., Spieldiedel A., Feautrier N., 2017, Mon. Not. R. Astronom. Soc., 471, 1849
Dunning T. H., 1989, J. Chem. Phys., 90, 1007
Dutrey A., Guilloteau S., Guélin M., 1996, Chemistry of Protosolar-like Nebulae: The Molecular Content of the DM Tau and GG Tau Disks
Endres C. P., Schlemmer S., Schilke P., Stutzki J., Müller H. S. P., 2016, Journal of Molecular Spectroscopy, 327, 95
Godard Palluet A., Lique F., 2023, J. Chem. Phys., 158, 044303
Gottlieb C. A., Gottlieb E. W., Thaddeus P., 1983, ApJ, 264, 740
Kalugina Y., Kłos J., Lique F., 2013, J. Chem. Phys., 139
Knowles P. J., Hampel C., Werner H. J., 1993, J. Chem. Phys., 99, 5219
Lampton M., Margon B., Bowyer S., 1976, ApJ, 208, 177
Linsky J. L., et al., 2006, ApJ, 647, 1106
Nagy Z., Ossenkopf V., Van der Tak F. F. S., Faure A., Makai Z., Bergin E. A., 2015, A&A, 578, A124
Najar F., Ben Abdallah D., Spieldiedel A., Dayou F., Lique F., Feautrier N., 2014, Chemical Physics Letter, 614, 251
Offer A. R., van Hemert M. C., van Dishoeck E. W., 1993, J. Chem. Phys., 100
Padovani M., Walmsley C. M., Tafalla M., Galli D., Müller H. S. P., 2009, A&A, 505, 1199
Parise B., Leurini S., Schlike P., Roueff E., Thorwirth S., Lis D. C., 2009, A&A, 508, 737
Roueff E., Lique F., 2013, Chem. Rev., 113
Sakai N., Saruwatari O., Sakai T., Takano S., Yamamoto S., 2010, A&A, 512
Sastry K. V. L. N., Helminger P., Charo A., Herbst E., De Lucia F. C., 1981, ApJ, 251, 119
Schöier F. L., Jørgensen J. K., van Dishoeck E. F., Blake G. A., 2002, A&A, 390, 1001
Spieldiedel A., Feautrier N., Najar F., Ben Abdallah D., Dayou F., Senent M. L., Lique F., 2012, Mon. Not. R. Astronom. Soc., 421, 1891
Teyssier D., Fossé D., Gerin M., Pety J., Abergel A., Roueff E., 2003, A&A, 417, 135
Treviño-Morales S. P., et al., 2014, A&A, 569
Tucker K. D., Kutner M. L., Thaddeus P., 1974, ApJ, 193, 115
Turner B. E., 2001, ApJ, 136, 579
Van der Tak F. F. S., Black J. H., Schöier F. L., Jansen D. J., van Dishoeck E. F., 2007, Mon. Not. R. Astronom. Soc., 468, 627
Van der Tak F. F. S., Lique F., Faure A., Black J. H., van Dishoeck E. F., 2020, Atoms, 8, 15
Vrtilek J. M., Gottlieb C. A., Langer W. D., Thaddeus P., Wilson R. W., 1985, A&A, 296, 35
Werner H. J., Knowles P. J., et al. F. R. M., 2020, J. Chem. Phys., 152
Wootten A., Bozyan E. P., Garrett D. B., Loren R. B., Snell R. L., 1980, ApJ, 239, 844
Yoshida K., Sakai N., Nishimura Y., Tokumode T., Watanabe Y., Sakai T., Takano S., 2019, Publ. Astron. Soc. Japan, 71
Ziurys L. M., Saykally R. J., Plambeck R. L., Erickson N. R., 1982, ApJ, 254, 94

APPENDIX A: DISCUSSION ON THE SCATTERING CONVERGED PARAMETERS

Fine-structure resolved cross sections for C_2H and C_2D in collision with both *ortho*- and *para*-H_2 were determined through solution of the CC equations. To do so, the rotational basis of the targeted molecule n_{max} and the total angular momentum J_{tot} are converged for different total energies E_{tot} at different energy steps ΔE. For all collisional systems, the rotational basis of the H_2 collider was chosen to be $j_{2,max} = 0,2$ for *para*-H_2 and $j_{2,max} = 1$ for *ortho*-H_2. The largest parameters are presented in Tables A1–A2. Optimization was done in order to converge cross sections within 1 percent of accuracy for each parameter. The propagation of the partial waves was done from $R_{min} = 4.25a_0$ to $R_{max} = 50a_0$ for C_2H collisions, and from $R_{min} = 4.25a_0$ to $R_{max} = 60a_0$ for C_2D collisions. Then, hyperfine calculations were done using the nuclear spin-free S-matrices computed with these parameters.

This paper has been typeset from a TEX/LATEX file prepared by the author.

Table A1. Values of the converged parameters used for scattering calculations for the C_2H–H_2 collisional system. The rotational basis n_{max} of the targeted molecule, total angular momentum J_{tot} and total energies E_{tot} with energy steps ΔE are presented.

C_2H–*ortho*-H_2				C_2H–*para*-H_2			
E_{tot} (cm^{-1})	ΔE (cm^{-1})	n_{max}	J_{tot}	E_{tot} (cm^{-1})	ΔE (cm^{-1})	n_{max}	J_{tot}
118.8–168.7	0.1	9	18	0.1–50	0.1	10	18
168.8–218.7	0.1	12	24	50.1–100	0.1	12	24
218.9–318.7	0.1	15	30	100.1–200	0.1	15	27
319.7–618.7	0.1	17	42	200.2–300	0.1	19	39
620.7–818.7	2	20	48	301–500	1	19	39
823.7–1118.7	5	24	57	505–700	5	22	45
1128.7–1618.7	10	27	69	710–1000	10	25	51
1718.7–2118.7	100	27	85	1050–1500	50	28	60
2318.7–3118.7	200	27	100	1600–2000	100	28	81
3618.7	500	27	100	2200–3000	200	28	100
				3500	500	28	100

Table A2. Values of the converged parameters used for scattering calculations for the C_2D–H_2 collisional system. The rotational basis n_{max} of the targeted molecule, total angular momentum J_{tot} and total energies E_{tot} with energy steps ΔE are presented.

C_2D–*ortho*-H_2				C_2D–*para*-H_2			
E_{tot} (cm^{-1})	ΔE (cm^{-1})	n_{max}	J_{tot}	E_{tot} (cm^{-1})	ΔE (cm^{-1})	n_{max}	J_{tot}
118.8–168.7	0.1	12	18	0.1–50	0.1	11	18
168.8–218.7	0.1	12	24	50.1–100	0.1	13	24
218.9–318.7	0.1	13	30	100.1–200	0.1	16	30
318.9–618.7	0.2	15	45	200.2–500	0.2	20	42
619.2–818.7	0.5	18	51	500.5–700	1	23	48
819.7–1118.7	1	21	57	705–1000	5	28	54
1123.7–1618.7	5	25	66	1010–1500	10	34	60